Contents lists available at ScienceDirect

Journal of Energy Storage

journal homepage: www.elsevier.com/locate/est

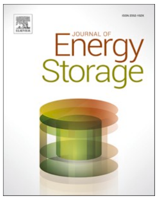

Research Papers

# Polymer derived SiOC/Sn nanocomposites from a low-cost single source precursor as anode materials for lithium storage applications

Gurdial Blugan [a,*], Natalia Kovalska [a,*], Dominik Knozowski [c], Pradeep V.W. Sasikumar [a], Wim J. Malfait [b], Silvia Paz [d], Piotr Madajski [e], Mateusz Leśniewski [f], Mirosław Sawczak [g], Balanand Santhosh [c], Monika Wilamowska-Zawłocka [c], Matthias M. Koebel [d]

[a] Laboratory for High Performance Ceramics, Empa, Swiss Federal Laboratories for Materials Science & Technology, CH-8600 Dübendorf, Switzerland
[b] Laboratory for Building Energy Materials and Components, Empa, Swiss Federal Laboratories for Materials Science & Technology, CH-8600 Dübendorf, Switzerland
[c] Department of Energy Conversion and Storage, Faculty of Chemistry, Gdańsk University of Technology, 80-233 Gdańsk, Poland
[d] Siloxene AG, CH-8306 Wangen-Bruttisellen, Switzerland
[e] Faculty of Chemistry, Nicolaus Copernicus University in Torun, 87-100 Toruń, Poland
[f] Laboratory of Functional Materials, Faculty of Electronics, Telecommunications and Informatics, Gdańsk University of Technology, 80-233 Gdańsk, Poland
[g] Institute of Fluid Flow Machinery, Polish Academy of Sciences, Fiszera 14, 80-231 Gdańsk, Poland

ARTICLE INFO

*Keywords:*
Q-T polysiloxane
Sn
Nanocomposites
Anode
Li-ion battery

ABSTRACT

Metal- based materials capable of lithium (Li) alloy formation are key to realization of the next generation of high-energy density anodes for Li-ion batteries, owing to their high storage capacity. Designing a good supporting matrix is essential for homogeneously nesting these metallic nanodomains, to effectively utilize their high capacity while tackling the volume expansion issues. Silicon oxycarbides (SiOC), obtained via a polymer derived approach, have recently gained interest as efficient host matrices. However, the high price and limited availability of the precursors for these ceramics present a challenge for their use at a commercial level. Sn nanoparticles, measuring less than 100 nm in size, are formed in-situ within the amorphous SiOC matrix using an economical single-source precursor. The polymeric precursor was indigenously developed from a novel, low cost vinyl functionalized polysiloxane and tin dioleate as the Sn source. Tin dioleate at different wt%, viz. 33–56 %, was uniformly crosslinked with the Q-T polysiloxane and was pyrolysed at 1000 °C in an argon atmosphere to obtain the SiOC/Sn nanocomposites. The electrochemical characterization of SiOC/Sn ceramic nanocomposite anodes exhibit outstanding specific capacities of 650 and 750 mAh $g^{-1}$ at 372 and 18.6 mA $g^{-1}$, respectively after 400 charge/discharge cycles.

## 1. Introduction

Research focusing into the development of alternative anodes for next generation lithium-ion improved performance has spurred intensive research into novel electrode materials. Si has emerged as a front-runner due to its high specific capacity, which significantly exceeds that of conventional graphite anodes in Li-ion batteries [1–4]. Compared to crystalline Si, silicon oxy carbides (SiOCs) obtain high structural stability, low volumetric expansion, ease of fabrication, and large-scale production capability [5]. In addition, the pyrolysis process produces varying degrees of disordered carbon (free carbon), which acts as an efficient charge carrier and active site for Li-ion insertion, further enhancing the electrochemical performance of SiOC anodes. The reported specific capacities of SiOC anodes range from 200 to 1300 mA h $g^{-1}$, reflecting structural differences in the SiOC ceramics used. The main challenge is its low columbic efficiency and the irreversible nature of alloying reactions between Li and Si.

Recent studies show that the lithium storage mechanisms of SiOC/Sn nanocomposites involve the reversible formation of the $Li_{22}Sn_5$ alloy during lithiation/delithiation, as confirmed by in situ XRD and ex situ

---

* Corresponding authors.

*E-mail addresses:* gurdial.blugan@empa.ch (G. Blugan), natalia.kovalska@empa.ch (N. Kovalska), dominik.knozowski@pg.edu.pl (D. Knozowski), wim.malfait@empa.ch (W.J. Malfait), s.paz@siloxene.com (S. Paz), piotr.madajski@doktorant.umk.pl (P. Madajski), mateusz.lesniewski@pg.edu.pl (M. Leśniewski), mireks@imp.gda.pl (M. Sawczak), balanand.santhosh@pg.edu.pl (B. Santhosh), monika.wilamowska@pg.edu.pl (M. Wilamowska-Zawłocka), m.koebel@siloxene.com (M.M. Koebel).

https://doi.org/10.1016/j.est.2024.111676
Received 10 January 2024; Received in revised form 28 March 2024; Accepted 8 April 2024

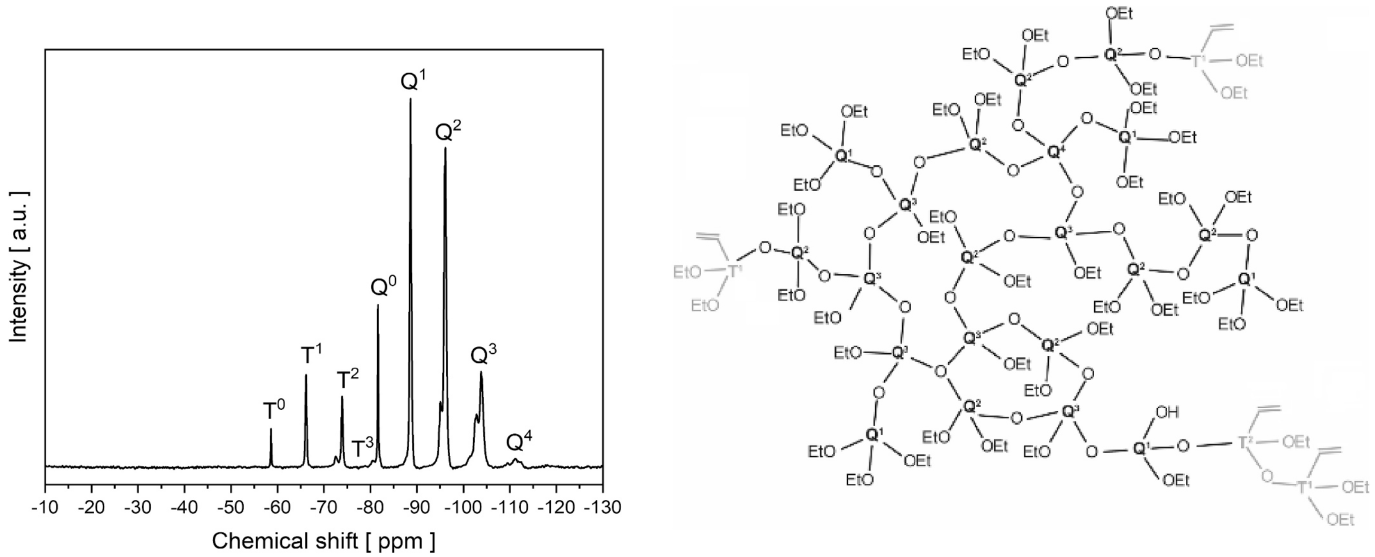

**Fig. 1.** $^{29}$Si NMR spectrum with signal assignments from a funPEOS core-shell product containing vinyl functional group.

TEM analyses [6]. This alloying process enables efficient lithium-ion accommodation without structural degradation, ensuring long-term stability. In addition, the uniform lithium ion diffusion pathways, maintained by the absence of significant Sn aggregation within the SiOC matrix, improve electrochemical performance and cycle life. Furthermore, the high rate capability of SiOC/Sn nanocomposites, due to synergistic effects between the SiOC matrix and dispersed tin nanoparticles, facilitates fast lithium ion diffusion kinetics and efficient electron transport. Collectively, these mechanisms contribute to excellent electrochemical performance as anode materials for lithium-ion batteries [6,7].

The pursuit to increase energy density at cell level has led to a significant shift in focus towards the investigation of alloyed anode materials [8]. The introduction of alloyed anode materials such as Sn and Si can reduce the dependency on graphite and also can deliver almost 3–10 times more storage capacity than conventional graphite anodes [9–11]. However, this high capacity comes with a drawback of volume expansion which is a major hurdle for the realization of these materials in commercial batteries. The incorporation of high capacity alloying materials within an active matrix is found to be an effective solution for realising high capacity and high rate capabilities of anode materials [6]. The synthesis of nanocomposites through a polymer derived ceramic (PDC) route provides a new insight for the realization of homogeneous metal-ceramic nanocomposite materials, where nano-sized particles of the active metals are dispersed within a silicon oxycarbide (SiOC) based ceramic matrix [12–15]. The SiOC based anode material itself can achieve a capacity of around 600 mA h g$^{-1}$, facilitate bulk buffering of volumetric changes, and significantly prevent the formation of an unstable solid-electrolyte interface [6]. This is due to its unique microstructure, which consist of a disordered free carbon domain within an amorphous SiOC tetrahedral environment [14]. Polymer derived SiOC/Sn$_x$ nanocomposites have gained attention to their high Li-storage capacities and rate capabilities [7]. Recent studies have demonstrated the advantages of SiOC/metal (Sn, Sb) nanocomposites in terms of electrical conductivity, cyclic stability and gravimetric lithium storage capacity, where the SiOC is functioning as the host matrix embedding metal nanoparticles [6,15].

A uniform SiOC matrix was essential, as in the case of the SiOC/Sn$_x$ nanocomposites, to prevent particle pulverisation and cracking at the rough solid/electrolyte interface [6]. Furthermore, the in-situ approach also facilitates the homogenous distribution of the metal nanoparticles in the PDC matrix via carbothermal reduction [6,15]. However, the challenges of high cost and availability need to be overcome to bring to market a new material based on PDC nanocomposites [16], which have numerous advantages over conventional anodes, to replace the widely used and low- priced graphite. In this work, a single source polymeric precursor system is synthesized by combining novel polysiloxanes with oxygen-rich metal precursors. This new type of hybrid vinyl functionalised Q-T polysiloxane or funPEOS is obtained by grafting vinylsilane monomers on polyethoxysiloxanes (PEOS) as building blocks resulting in homogeneously distributed vinyl groups decorating the outer periphery of the functional PEOS molecules (funPEOS) [17]. The core-shell design in characterized by no sharp boundary division between core and shell, but a more diffuse distribution of functional silanes at the surface. Such functional PEOS offer processing and logistical advantages due to their low solution viscosity, high solids content and non-flammable nature. Furthermore, compared to functional D-type (modified PDMS) polysiloxane precursors, the Q-T chemistry offers significant advantages in terms of cost savings, because organofunctional D-type precursors are often costly and not commercial at scale. Exploring a range of different functionalities to compatibilize transition metal doped SiOC precursor applications is challenging, but the universal nature of the technology offers innumerable possibilities for targeted application benefits. The versatility and the comparably lower cost of funPEOS compared to specialty D-type silicone precursors is a great benefit for many potential applications, including its role as a potential co-precursor for battery anode materials, which is the main focus of this study.

## 2. Experimental

### 2.1. *Synthesis of funPEOS siloxane*

A novel polymeric liquid vinyl-functional QT-polysiloxane material XenCure V35 with a vinyl-group loading of 1 mmol/g was provided by Siloxene AG, Switzerland [17]. The preparation includes a two-step process: (1) the PEOS (Q-type) precursor is first prepared using non-hydrolytic condensation chemistry followed by (2) grafting of the organofunctional silane VTMS (vinyltrimethoxysilane) on the surface of the PEOS dendrimer [18]. The molar mass and the size of the PEOS precursor can be adjusted by stoichiometric control of the ratio of acetic anhydride to silane monomer on both steps (1) and (2).

According to [17], functionalized polyethoxysiloxane (funPEOS) can be synthesized from hyperbranched polyethoxysilane cores based on tetraethyl orthosilicate followed by the addition of a vinyl silane with high functional group loading to create the vinyl functional shell chemistry needed for further radical polymerisation during preparation

**Table 1**
Composition of the starting precursors used in the preparation of SiOC/$Sn_x$ nanocomposites.

| Name | funPEOS [g] | $Sn(Ole)_2$ [g] | HDDA [g] | DCP [g] |
|---|---|---|---|---|
| SiOC/Sn-1 | 2 | 1.0 | 0.5 | 20 |
| SiOC/Sn-1.5 | 2 | 1.5 | 0.5 | 20 |
| SiOC/Sn-2 | 2 | 2.0 | 0.5 | 20 |
| SiOC/Sn-2.5 | 2 | 2.5 | 0.5 | 20 |

of the hybrid SiOC preceramic green body. A $^{29}$Si NMR spectrum and a symbolic molecular formula of the XenCure V35 funPEOS are shown in Fig. 1. Its molecular architecture is designed prior to synthesis by selecting the stoichiometry and process parameters to achieve the desired properties of the product, in this case a highly functional compact dendrimer which can be easily polymerized by heat in the presence of a suitable radical initiator. $^{29}$Si NMR spectroscopy reveals signals belonging to the ethylsilicate (PEOS) core precursor and the functional vinyl-alkoxysilane shell ($T^n$) appearing as clearly separated spectral regions including their differently bonded molecular moieties ($Q^0$-$Q^4$ and $T^0$-$T^3$). Both PEOS and funPEOS compounds are stable in organic liquids and have a nearly unlimited shelf-life if stored properly.

## 2.2. Synthesis of SiOC/Sn nanocomposites from funPEOS siloxane

The development of a nanocomposite with homogeneously distributed metallic tin nanodomains within a glassy SiOC network is described. A radical cross-linked Q-T siloxane (funPEOS)/Sn based preceramic network, was prepared by radical polymerisation of a blend containing the XenCure V35 funPEOS (siloxene AG, Switzerland) with different amounts of Sn dioleate ($Sn(Ole)_2$) (Sigma Aldrich, Germany). The addition of the $Sn(Ole)_2$ served as a source of C and Sn in the final ceramic nanocomposite. Several compositions of funPEOS (SiOC precursor) and $Sn(Ole)_2$ (tin precursor) were prepared in different mass ratios of Sn precursor $(SnOle)_2$ to SiOC precursor (funPEOS), SiOC/$Sn_x$ (viz. 2:1; 2: 1.5; 2: 2; 2: 2.5), and are hence named SiOC/Sn-1, SiOC/Sn-1.5, SiOC/Sn-2, and SiOC/Sn-2.5, respectively. 1,6-Hexanediol diacrylate (HDDA) (Sigma-Aldrich, Germany), was used as a radical curing crosslinker and dicumylperoxide (DCP) (Sigma-Aldrich, Germany), as the radical initiator (see Table 1 for more details regarding the precursor composition).

The precursor compounds were mixed together with the curing agent and the radical initiator at 140 °C using a magnetic stirrer. The mixture was stirred continuously for 15–20 min until the resulting suspension changed its colour from transparent white to yellow and became more viscous. At this stage, the heating was reduced to the temperature of 80 °C, due to the intense exothermic polymerisation. The polymerized solid green bodies (cross-linked preceramic complex) were aged inside a drying cabinet at 140 °C for 24 h. The cross-linked precursor mixtures were light yellow in colour, transparent, and appeared single-phase to the naked eye. The polymer-to-ceramic transformation of these copolymerized vinylsiloxane/HDDA/tin dioleate preceramics was carried out in an alumina tubular furnace (Carbolite, Germany) at a temperature of 1000 °C with dwell time of 1 h and a heating rate of 3 °C/min, under an argon atmosphere.

## 2.3. Characterization techniques

$^1$H-$^{29}$Si Cross Polarisation Magic Angle Spinning ($^1$H-$^{29}$Si CPMAS) Nuclear Magnetic Resonance (NMR) spectra of preceramic green bodies [19,20] were acquired with a Bruker Avance III spectrometer equipped with a 9.4 T wide-bore magnet (400.2 and 79.5 MHz Larmor frequencies for $^1$H and $^{29}$Si, respectively), inside 7 mm rotors, with a 4 kHz MAS rate, a recycle delay of 3 s, and a relatively long contact time of 5 ms to minimize the dependencies of the relative spectral intensities on the H to Si distance.

A Netzsch STA449 F3 Jupiter (Germany) instrument was used for differential scanning calorimetry/thermal gravimetric analysis (DSC/TGA). The experiments were carried out in an argon atmosphere at a flux of 250 ml/min, and at a heating rate of 5 °C/min up to 1000 °C.

Attenuated total reflectance FTIR spectra were recorded using a Bruker Tensor 27 spectrometer (Bruker, USA) equipped with a Golden Gate ATR crystal. Raman analysis was performed using a micro-Raman spectrometer (InVia, Renishaw, Wotton-under-Edge, UK) equipped with an Ar ion laser (514 nm) in the range 100–3200 $cm^{-1}$. The analysis of the obtained spectra was performed using OriginPro2016 software after background subtraction with custom settings. The spectra were deconvoluted using Lorentzian type peak for the D4, D1, G, and D2 bands, and Gaussian type peak for the D3 band [21].

The structural analysis and phase identification was studied by X-ray diffraction (XRD) in Bragg–Brentano geometry using a BRUKER AXS D8 ADVANCE diffractometer equipped with a Cu-Kα X-ray source. The data were acquired in the 2θ range of 5–120° with a step of 0.02° and a 1 s exposure time per step.

The content of C and Sn in the SiOC/$Sn_x$ was determined by elemental analysis at the Mikroanalytisches Labor Pascher (Remagen-Bandorf, Germany). For the C detection the sample was combusted at 1100 °C – 1200 °C in a purified oxygen stream, where the resulting carbon dioxide was absorbed in 0.1 N NaOH and detected conductometrically. The Sn was detected by ICP-AES (Inductively Coupled Plasma - Atomic Emission Spectroscopy) after digestion.

The morphology of the materials was characterized using a scanning electron microscope SEM (Tescan VEGA, Tescan, Brno, Czech Republic) and a transmission electron microscope TEM (FEI, G2 F20X-Twin 200 kV, FEG). The surface elemental distribution was evaluated using a Phenom XL Scanning Electron Microscope (ThermoFisher Scientific, Warsaw, Poland) equipped with an energy dispersive X-ray (EDX) microanalyser.

Electrochemical measurements were performed using a multi-channel battery tester (Neware BTS4000 series, Neware Technology Limited, China) and on the Biologic Potentiostat SP200 (BioLogic Science Instruments, Seyssinet-Pariset, France) in a half-cell configuration (Swagelok® type cells). The electrode preparation steps were as follows: the finely grounded active material (SiOC/Sn nanocomposite, 85 wt%) was mixed with the conductive additive (carbon black, Super C-65, Imerys Graphite & Carbon, Switzerland, 7.5 wt%) and homogenized in a ball mill for 1 h at 25 Hz (10 ml zirconia mill with 20 zirconia balls (diameter of 5 mm), Mixer Mill, MM200, Retsch, Germany). The binder solution (carboxymethyl cellulose, CMC, SUNROSE MAC 500LC, Nippon Paper Group, 7.5 wt%) in water was then added to the active material/carbon black mixture, and the components were further homogenized for 1.5 h. The obtained slurry was cast on a Cu foil (oxygen-free copper foil SE-Cu58, hard as rolled, Cu-treatment on both sides, Schlenk Metallfolien GmbH & Co. KG, Germany) using the doctor blade technique (100 μm wet layer). The layers were dried overnight in a vacuum oven at 120 °C. The loading of active electrodes (diameter of 10 mm) was in a range of 1.5 and 2 mg $cm^{-2}$. The electrochemical cells were prepared using 1 M $LiPF_6$ in EC:DMC (ethylene carbonate: dimethyl carbonate, 1:1 v:v) as electrolyte (Sigma Aldrich, Germany), glass microfiber separator (MN GF-2, Macherey-Nagel GmbH & Co. KG, Düren, Germany, thickness 45 μm), and lithium foil (Sigma Aldrich, Schnelldorf, Germany) as the counter/reference electrode. The cells were measured after a waiting time of approx. 20 h. The galvanostatic charge–discharge cycles were performed using the constant current–constant voltage (CCCV) protocol in the potential range of 0.005 V–1.5 V with a potential hold of 15 min after the lithiation step. Cyclic voltammetry (CV) measurements were conducted with a scan rate of 0.1 mV $s^{-1}$ within the same potential range.

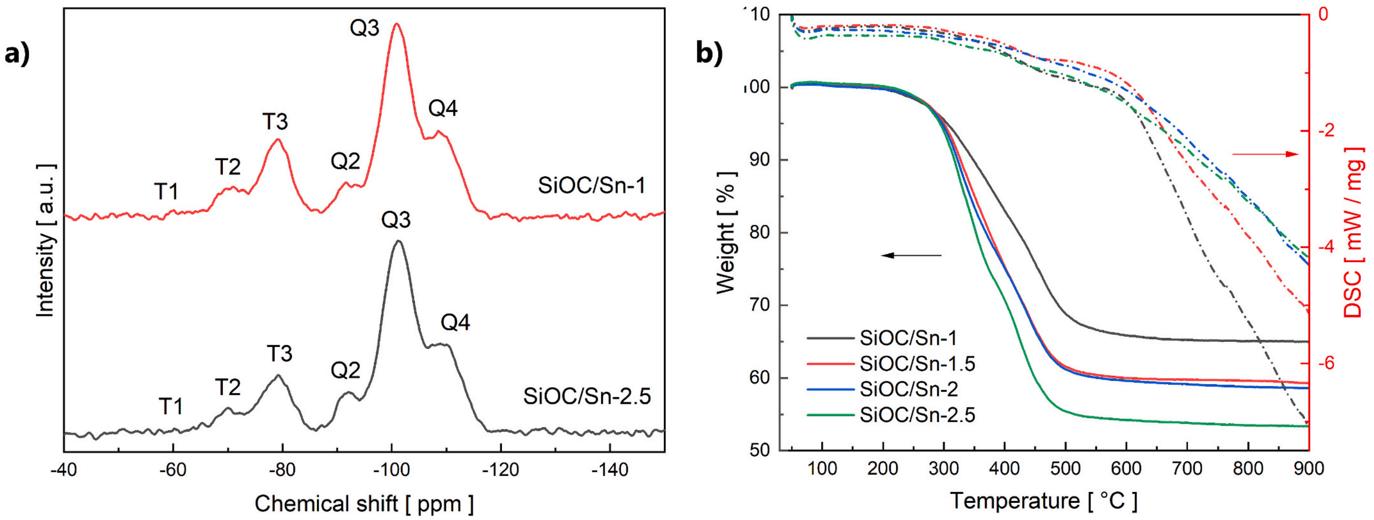

**Fig. 2.** a) Solid-state $^{1}$H-$^{29}$Si CP MAS NMR of SiOC/Sn preceramic complex and b) TG/DSC analysis of the SiOC/Sn nanocomposite precursor, performed in argon with a heating rate 5 °C/min.

## 3. Results and discussions

### 3.1. Analysis of the Sn-modified siloxane (preceramic complex)

The SiOC/Sn$_x$ ceramic precursors were synthesized by incorporating different amounts of Sn(Ole)$_2$ to obtain the different compositions, with increasing active Sn metal loading. Two of the Sn modified precursors, expected to have the highest (SiOC/Sn-2.5) and lowest (SiOC/Sn-1) Sn content in the polymeric architecture, were analysed with $^{1}$H—$^{29}$Si CP MAS NMR, and the results are shown in Fig. 2a. The $^{1}$H—$^{29}$Si CP MAS NMR spectra for both compositions, SiOC/Sn-1 and SiOC/Sn-2.5 show similar behaviour with the peaks related to T$^{1}$, T$^{2}$ and T$^{3}$ (−60, −70 and − 80 ppm) with the strongest signal from T$^{3}$, indicative of a relatively high degree of polymerisation. No significant differences in the NMR signals were observed with different amounts of the Sn precursor. The positions of the T peaks are shifted quite far towards the right (i.e. towards the Q peaks), consistent with a vinyl/benzyl type R-group on the T-silane. The Q$^{2}$, Q$^{3}$ and Q$^{4}$ peaks at around −90, −100 and − 110 ppm are also present. The strongest peak is for Q$^{3}$ with a weaker signal for Q$^{4}$, but it is well known that Q$^{4}$ is underestimated heavily because of the cross-polarisation (CP) due to the absence of the close hydrogen atoms. Therefore, we can estimate that average connectivity on each Si atom is about ~3.2, as expected for silicate type glass materials.

Thermogravimetric analysis (TGA) and differential scanning calorimetry (DSC) were carried out to understand the pyrolysis mechanism of the SiOC/Sn$_x$ nanocomposites (see Fig. 2b). The TGA curves show mass loss in the temperature range of ~200 °C to ~550 °C, which continues to a plateau. The mass loss in this temperature range is attributed to the release of volatile compounds during pyrolysis, resulting in a mass reduction of ~35 wt% for SiOC/Sn-1; ~40 wt% SiOC/Sn-1.5; ~42 wt% SiOC/Sn-2 and up to 48 wt% for SiOC/Sn-2.5. The DSC curve shows a slight decrease around 450 °C, which is attributed to the carbothermal reduction of Sn formed during decomposition of Sn(Ole)$_2$ [6]. Although the samples were prepared with the corresponding amount of the Sn(Ole)$_2$ in the ratio of 0.5 wt%, however both SiOC/Sn-1.5 and SiOC/Sn-2 demonstrate similar trends, which suggests incomplete carbothermic reduction. On further heating, the DSC curve shows a significant drop around 650 °C, due to morphological phase transition from the preceramic (polymeric) to ceramic.

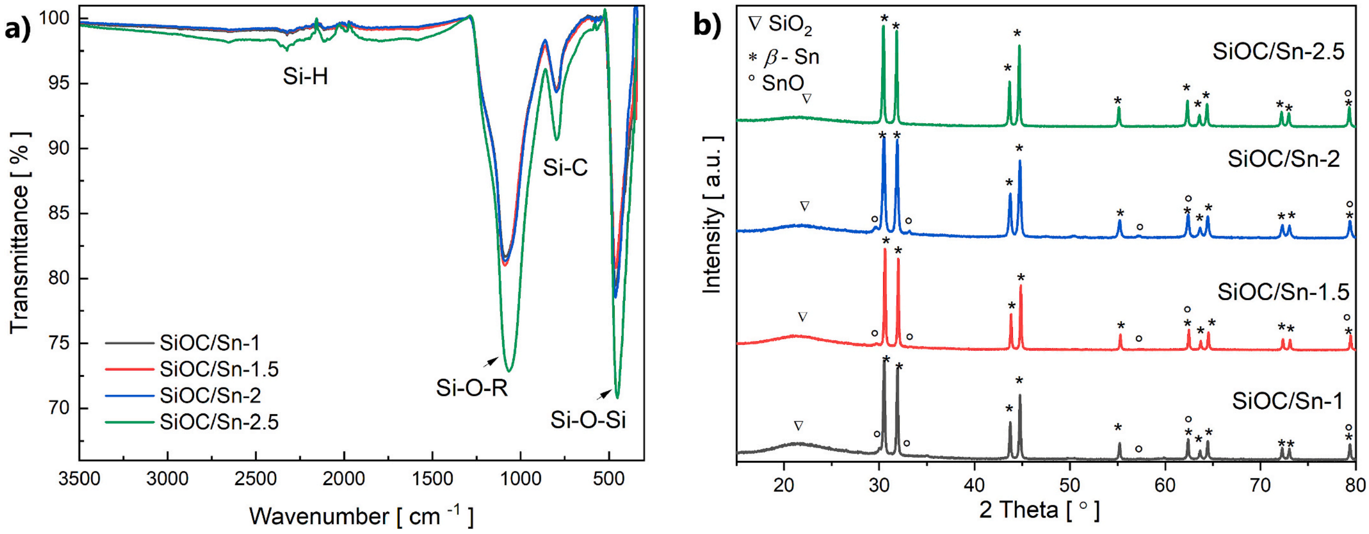

**Fig. 3.** a) FTIR analysis and b) XRD pattern. Compositions of SiOC/Sn: SiOC/Sn-1; SiOC/Sn-1.5; SiOC/Sn-2 and SiOC/Sn-2.5.

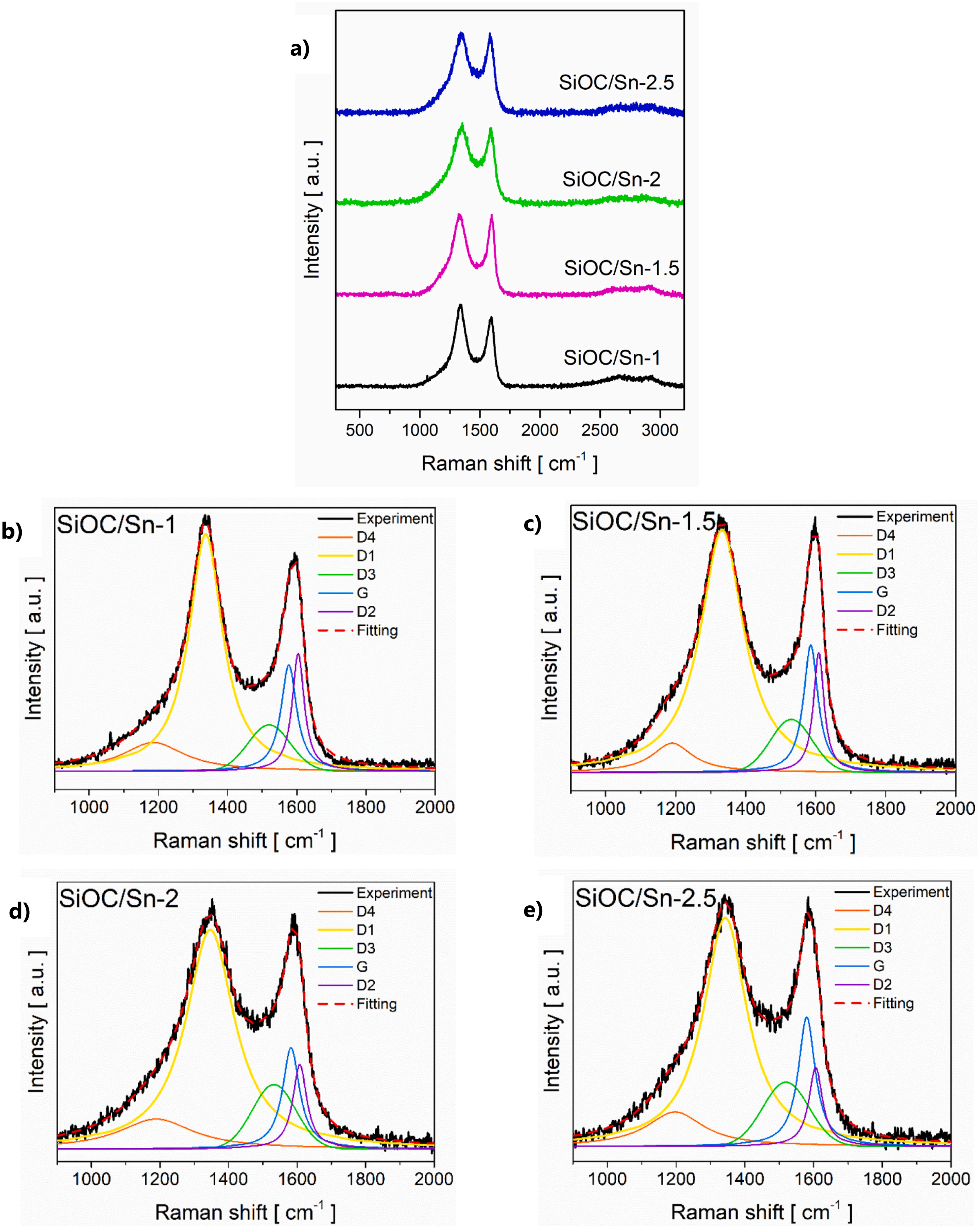

**Fig. 4.** Raman spectra of a) SiOC/Sn composite materials after background subtraction, fitting results for b) SiOC/Sn-1, c) SiOC/Sn-1.5, d) SiOC/Sn-2, and e) SiOC/Sn-2.5.

### 3.2. *Analysis of the SiOC/Sn ceramic nanocomposites*

Fourier infrared absorption spectroscopy (FTIR) was used to analyze the bonding phases derived from the different pre-ceramics, as shown in Fig. 3a. The absorption peaks observed at 1080 cm$^{-1}$ and in the vicinity of the 490 cm$^{-1}$ region typically indicate the presence of Si-O-Si bonds within the matrix [6,12]. Although, in this context the Si-O-R represents the Si—O bonds in the polymer backbone, where ‘R’ is a general representation of the functional group. The variable ‘R’ refers to any hydrocarbon group or other silicon chains attached to it in the preceramic form. In addition, mixed phases of the SiOC type overlap, in which some of the bridging oxygen atoms of the $SiO_2$ tetrahedra are substituted with carbon at 800 cm$^{-1}$. This indicates the presence of SiOC ceramic material in the structure after pyrolysis for all studied composites.

**Table 2**
Data from the deconvolution of Raman spectra of SiOC/$Sn_x$ nanocomposites.

| Sample | D4 | | D1 | | D3 | | G | | D2 | | $I_{D1}/I_G$ | $I_{D2}/I_G$ |
|---|---|---|---|---|---|---|---|---|---|---|---|---|
| | $cm^{-1}$ | inten. | $cm^{-1}$ | inten. | $cm^{-1}$ | inten. | $cm^{-1}$ | inten. | $cm^{-1}$ | inten. | | |
| SiOC/Sn-1 | 1185 | 0.112 | 1336 | 0.925 | 1520 | 0.181 | 1576 | 0.415 | 1603 | 0.459 | 2.23 | 1.11 |
| SiOC/Sn-1.5 | 1190 | 0.115 | 1332 | 0.935 | 1523 | 0.194 | 1586 | 0.509 | 1609 | 0.457 | 1.83 | 0.90 |
| SiOC/Sn-2 | 1191 | 0.123 | 1346 | 0.858 | 1525 | 0.234 | 1582 | 0.428 | 1608 | 0.337 | 2.00 | 0.79 |
| SiOC/Sn-2.5 | 1197 | 0.135 | 1342 | 0.897 | 1519 | 0.252 | 1579 | 0.507 | 1605 | 0.310 | 1.77 | 0.61 |

Furthermore, there were no prominent peaks or shift in peak positions in the spectra when the Sn content was increased in the samples. To confirm the presence of metallic Sn and to investigate the presence of other possible phases in the samples, X-ray diffraction analysis was carried out (Fig. 3b).

The performed XRD measurements identified multiple phase formation of β-Sn, SnO, and amorphous $SiO_2$ phases. The small hump within the amorphous peak range of 15–27° represents the characteristic amorphous silica phase commonly found in SiOC. The sharp peaks, which correspond to the β-Sn phase that represent a nanocrystallite structure [15]. The identified SnO phase indicates an incomplete carbothermal reduction during the pyrolysis, which may affect the electrochemical properties and reproducibility of the SiOC/Sn nanocomposites. This may be due to the high activation energy for the carbothermal reduction of Sn with carbon. However, it can be observed that the SnO phase is no longer present in SiOC/Sn-2.5.

The trends of quantitative integration of C and Sn elements, which is the main source of added $Sn(Ole)_2$, was studied by conductometric method for C and by inductively coupled plasma atomic emission spectroscopy to determine Sn. For a better comparison, the measurements were carried out on the samples with the highest and lowest amounts of added $Sn(Ole)_2$ (Table 1), which are represented by SiOC/Sn-2.5 and SiOC/Sn-1 samples, respectively. The measurements showed an increase in the carbon content from 6.01 ± 0.01 wt% to 9.11 ± 0.01 wt%, representing an increase of up to 3.1 wt%. For the Sn, the change was from 8.43 ± 0.02 wt% to 15.0 ± 0.03 wt% which represents an increase of up to 6.57 wt%. The measurements confirmed a quantitative integration of all non-volatile constituents, in particular Sn, in the final developed nanocomposite.

Raman measurements provided further insight into the structure of the carbon in the SiOC/$Sn_x$ nanocomposites. The Raman spectra of the investigated samples show D and G bands at ~1340 $cm^{-1}$ and ~ 1580 $cm^{-1}$, which are typical for carbonaceous materials (see Fig. 4). These modes were deconvoluted into five peaks for further examinations [21] (Fig. 4b–e). SiOC/$Sn_x$ nanocomposites show a typical SiOC response with a strong D1 band ($I_{D1}$ = 0.925–0.858), related to the disordered forms of carbon and much weaker G and D2 band intensities ($I_G$ = 0.507–257) and ($I_{D2}$ = 0.457–0.310), corresponding to the ideal and damaged graphitic lattice, respectively [21,22]. The increase of the Sn content in SiOC resulted in a decrease in the intensity of the D2 band and slight decrease in the D1 band intensity and a slight increase in the intensity of the D4 and D3 bands. The D4 band can be attributed to $Csp^2$-

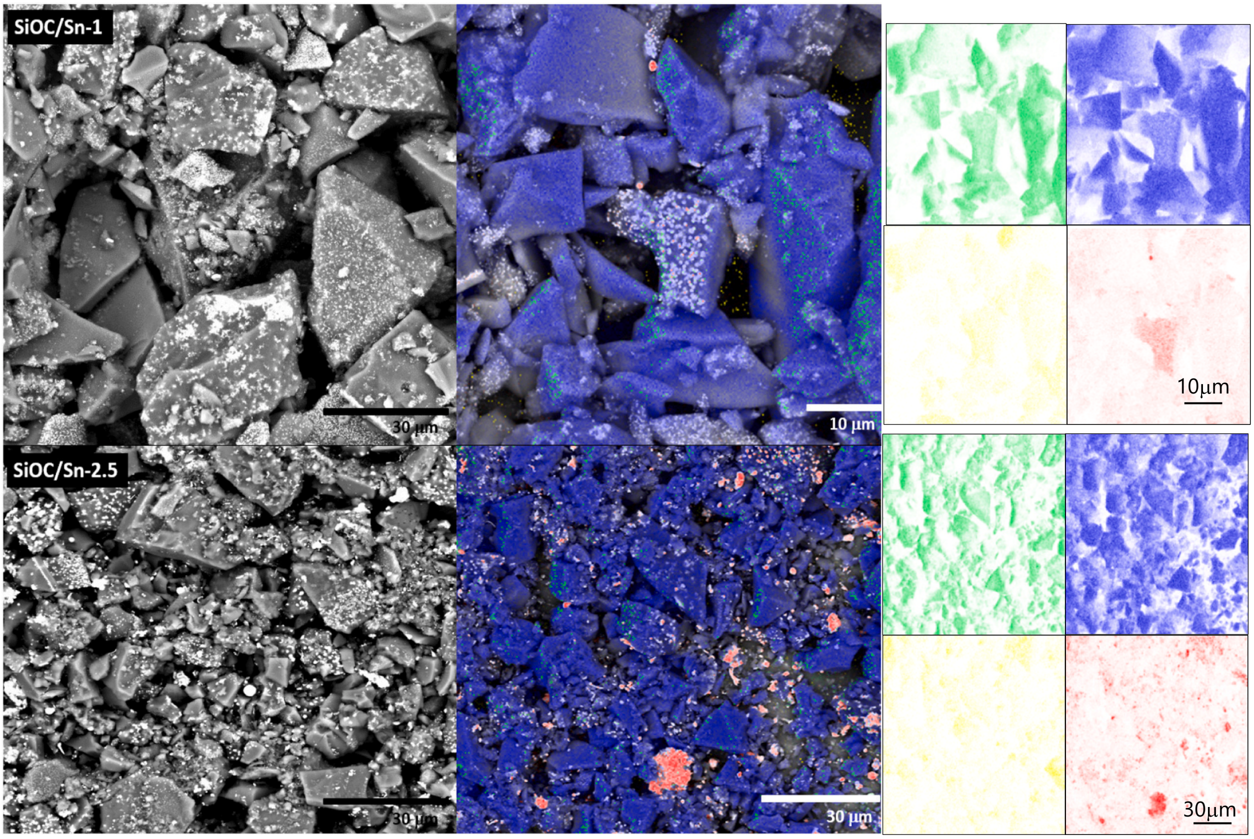

**Fig. 5.** SEM/EDX images of the SiOC/Sn-1 and SiOC/Sn-2.5 nanocomposites. Elemental mapping of Si-blue; Sn-red; O-green; C-yellow. The quantitative estimation of Sn content in several regions can be found in Table S2 (supplements). (For interpretation of the references to colour in this figure legend, the reader is referred to the web version of this article.)

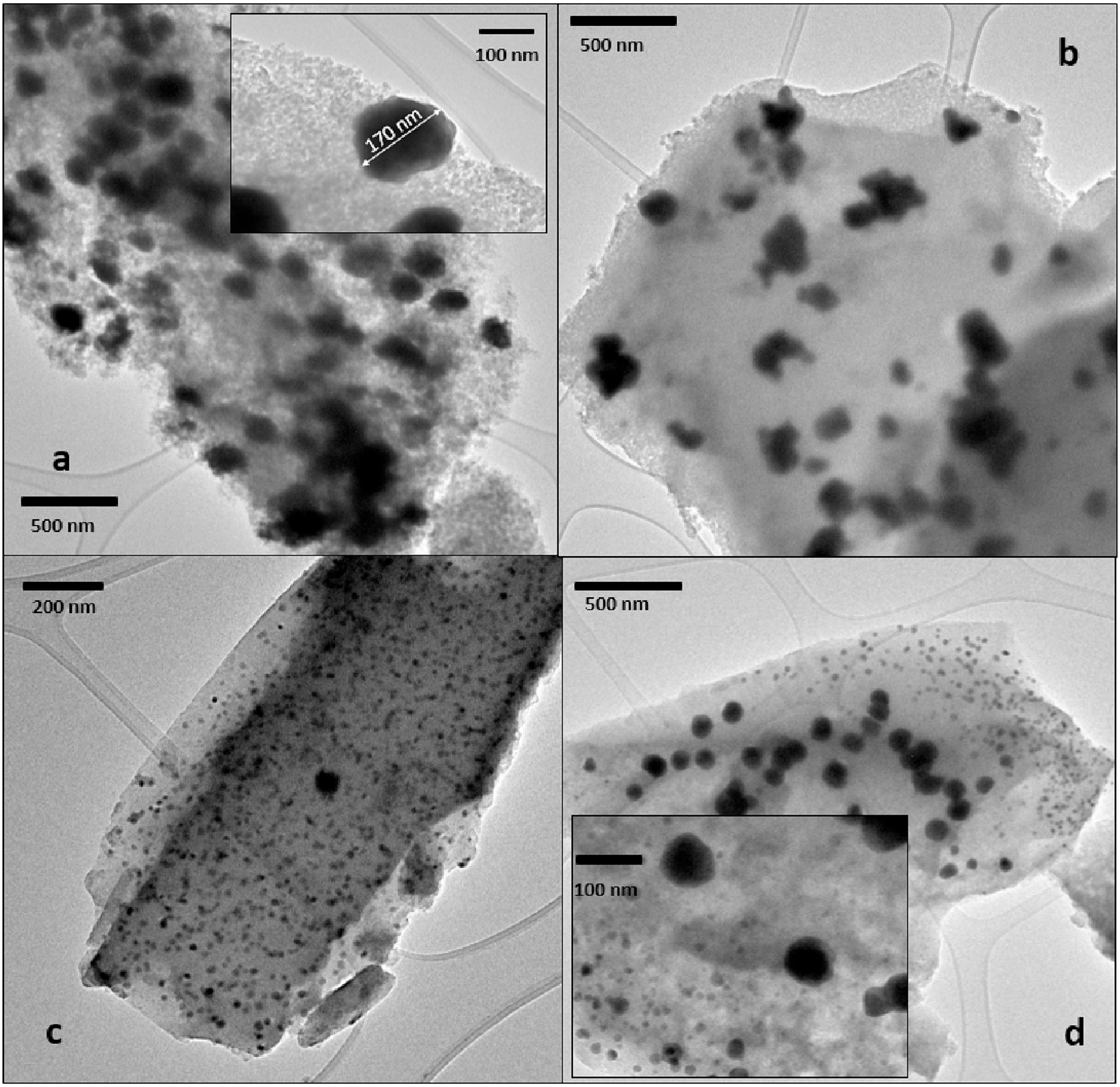

**Fig. 6.** TEM images of the SiOC/Sn$_x$: a) SiOC/Sn-1, b) SiOC/Sn-1.5, c) SiOC/Sn-2, and d) SiOC/Sn-2.5 nanocomposites.

Csp$^3$ bonds [23] or ionic impurities [24], while the D3 band is attributed to amorphous carbons. The presence of tin oxide in the composites could explain the presence of ionic dopants in the samples, which could give a rise to the D4 band. The analysed intensity ratios, $I_{D1}/I_G$ and $I_{D2}/I_G$, decrease with the increasing of the tin content in the ceramic matrix (Table 2). The $I_{D1}/I_G$ ratio decreases from 2.23 (SiOC/Sn-1 sample) to 1.77 (SiOC/Sn-2.5 sample), while the $I_{D2}/I_G$ ratio reduces from 1.11 (SiOC/Sn-1 sample) to 0.61 (SiOC/Sn-2.5 sample). The decrease in the $I_D/I_G$ ratios indicates a higher fraction of ordered carbon in the sample with the highest Sn content (SiOC/Sn-2.5), due to the carbothermal reduction process of tin oxide, which mainly consumes the disordered free carbon phase. This is in agreement with our previous observation for ternary SiOC/graphite/Sn composites [25].

The morphology and structure of the SiOC/Sn$_x$ nanocomposites were investigated using SEM/EDX and TEM analyses, presented in Figs. 5 and 6, respectively.

The SiOC/Sn-1 and SiOC/Sn-2.5 nanocomposites within the SiOC/Sn$_x$ group were compared using the SEM/EDX mapping analysis (see Fig. 5). These two samples showed significant differences in their morphologies. However, from the EDX analysis, the distribution of the oxygen (green), silicon (blue), and carbon (yellow) were observed in both measured nanocomposites. The SiOC/Sn-1 sample contained of spherical nanoparticles of Sn (indicated in pink on the EDX map), clustered in some areas, in a Si (shown in blue) rich matrix. Some spherical agglomerates of Sn, of sizes in the range of ~1.0–1.5 μm, were also observed in the SiOC/Sn-1 matrix. A similar trend was observed also in the case of SiOC/Sn-2.5; however, with more distributed and heterogeneous agglomerates up to ~15 μm. To understand the nature of the Sn distribution and clusters formation in the SiOC matrix, it was necessary to analyze the samples using a TEM.

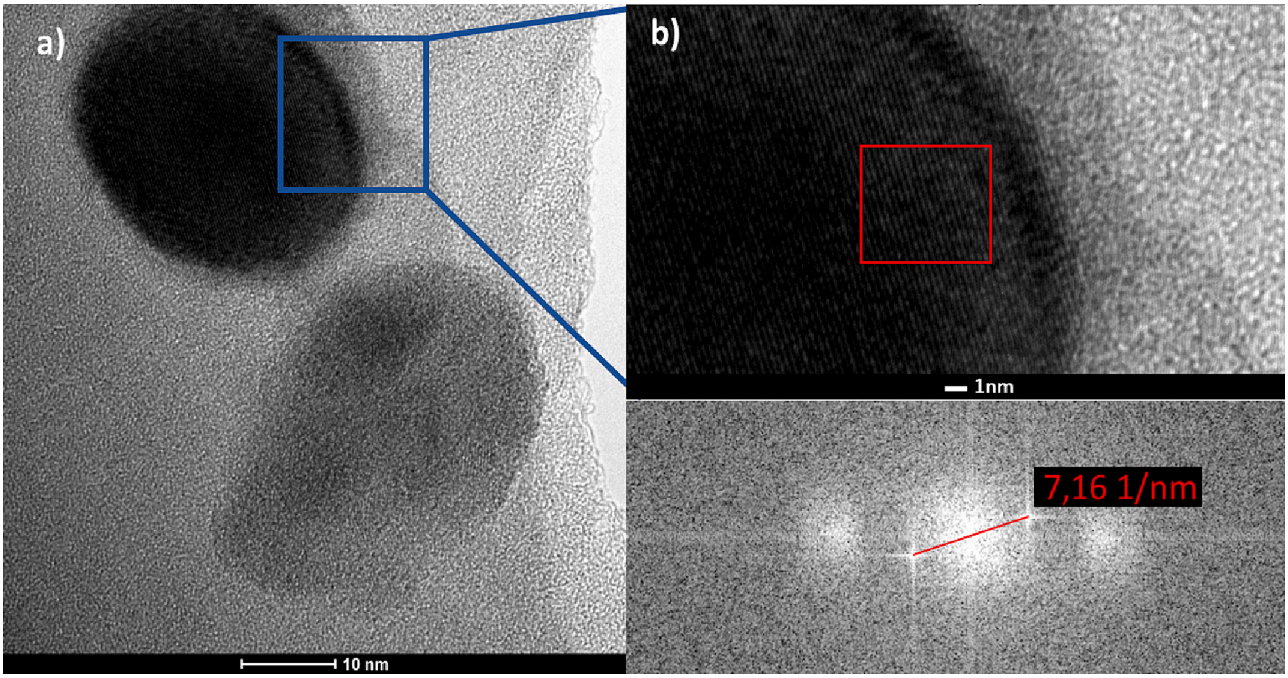

**Fig. 7.** Image of SiOC/Sn-2 sample: a) HRTEM, b) FFT diffraction pattern of the area marked in red. (For interpretation of the references to colour in this figure legend, the reader is referred to the web version of this article.)

TEM analysis was carried out for all the four compositions within the SiOC/$Sn_x$ nanocomposites system to investigate the Sn distribution in the SiOC matrix. The TEM analysis showed the presence of spherical Sn nanoparticles, observed as black spots in Fig. 6, homogenously dispersed in the ceramic matrix. This is in agreement with the SEM observation (as in SiOC/Sn-1). In the case of SiOC/Sn-1 and SiOC/Sn-1.5 composites, Sn nanoparticles of a similar size of about ~ 120–170 nm were well distributed in the ceramic matrix. While, in the case of the SiOC/Sn-2, smaller particles (size in the range ~10–20 nm along with a few number of particles of size ~150 nm) were investigated but with a better distribution of particles in the SiOC matrix. TEM analysis confirms the presence of particles of both sizes in the SiOC/Sn-2.5 sample, indicating some heterogeneity.

Based on the FFT diffraction pattern (see Fig. 7), the periodic arrangement has a plane space of about 0.279 nm, which corresponds to the (101) planar spacing of Sn.

## 4. Electrochemical measurements of the SiOC/$Sn_x$ nanocomposites

Nyquist plots were recorded for freshly prepared electrochemical cells at a standby potential Es of about 3 V, after first lithiation at 0.150 mV, and after 50 charge-discharge cycles in a lithiated state. Electric equivalent circuits (EEC) were fitted for all recorded spectra. Examples of fitting plots are shown in the insets of Fig. 8a–c. The resistance of the electrolyte, marked as *R*1 in EEC, was approximately 3.5 Ω for fresh cells and 3.5–4.5 Ω after 50 cycles. The charge-transfer resistance (*R*2) values for the fresh electrodes range from 60 to 100 Ω. After the first lithiation, as shown in Fig. 8b, the Warburg impedance at low frequencies becomes more pronounced, revealing the diffusion of lithium ions through the SiOC/$Sn_x$ nanocomposites. An additional (*RC*) element appears in the EEC for the lithiated samples, which may represent the formation of a solid-electrolyte interphase (SEI) layer. The *R* values from the EEC are presented in (Supplementary Table S2). It is worth noting that the charge transfer resistance values gradually decrease with cycling. After 50 charge-discharge cycles, they are significantly lower for all samples, which is evident from the lower diameter of the semicircle (refer to Fig. 8c). The decrease in resistance values may be attributed to the establishment of $Li^+$ diffusion pathways within the nanocomposites and the electrochemical activity arising from all the active components, namely SiOC, Sn nanoparticles, and tin oxide. The decrease in charge transfer resistance following cycling indicates that the composite electrodes are stable. This suggests that SiOC is a suitable matrix for alloying nanoparticles, which prevents excessive volume expansion and irreversible morphological and structural changes.

The electrochemical behaviour of the SiOC/$Sn_x$ nanocomposites, studied by cyclic voltammetry (CV), is shown in Fig. 9a. On the cathodic side, two main peaks were registered: first, at ~0.37 V corresponds to the initial tin alloying process, and the second, at ~0–0.16 V, is related to both: lithiation of silicon oxycarbide and formation of lithium-rich $Li_xSn$ compounds [26,27]. During the reverse sweep, four characteristic peaks appear between 0.46 and 0.8 V, which can be attributed to the stepwise delithiation of lithium from tin alloys [26]. The studied SiOC/$Sn_x$ nanocomposites obtained visually identical positions of the peaks, while the intensities of the peaks are proportional to the Sn precursor content used for the synthesis (see inset in Fig. 9a and Table 1). The shapes of the CV curves confirm the electrochemical activity of both SiOC and Sn, and furthermore, suggests electrochemical behaviour is directly related to the Sn content in the composites.

Fig. 9b shows the voltage profiles of the obtained SiOC/$Sn_x$ nanocomposites. The solid lines represent the first charge-discharge cycle, while the dashed ones the second cycle. The voltage profiles reveal distinct plateaus at 0.4 V during the lithiation process, and at 0.56–0.76 V on the delithiation curve, confirming multiple alloying steps. The voltage profiles are rather smooth and long-lasting, which suggests gradual lithiation processes in the SiOC/$Sn_x$ nanocomposite materials, representative of these material types [6,25,28]. The initial lithiation capacity values are ~ 1300–1500 mAh $g^{-1}$, while delithiation capacities are in the range of 600–700 mAh $g^{-1}$ (the exact values are collected in Table 3). The first cycle efficiencies are around 43–50 %, with the highest value of 51 % recorded for the SiOC/Sn-2 sample. The cycle efficiency steadily increases and reaches values above 99 % after a few cycles. A low first cycle efficiency (FCE) is a typical drawback of SiOC-based materials [7], and the addition of Sn does not significantly

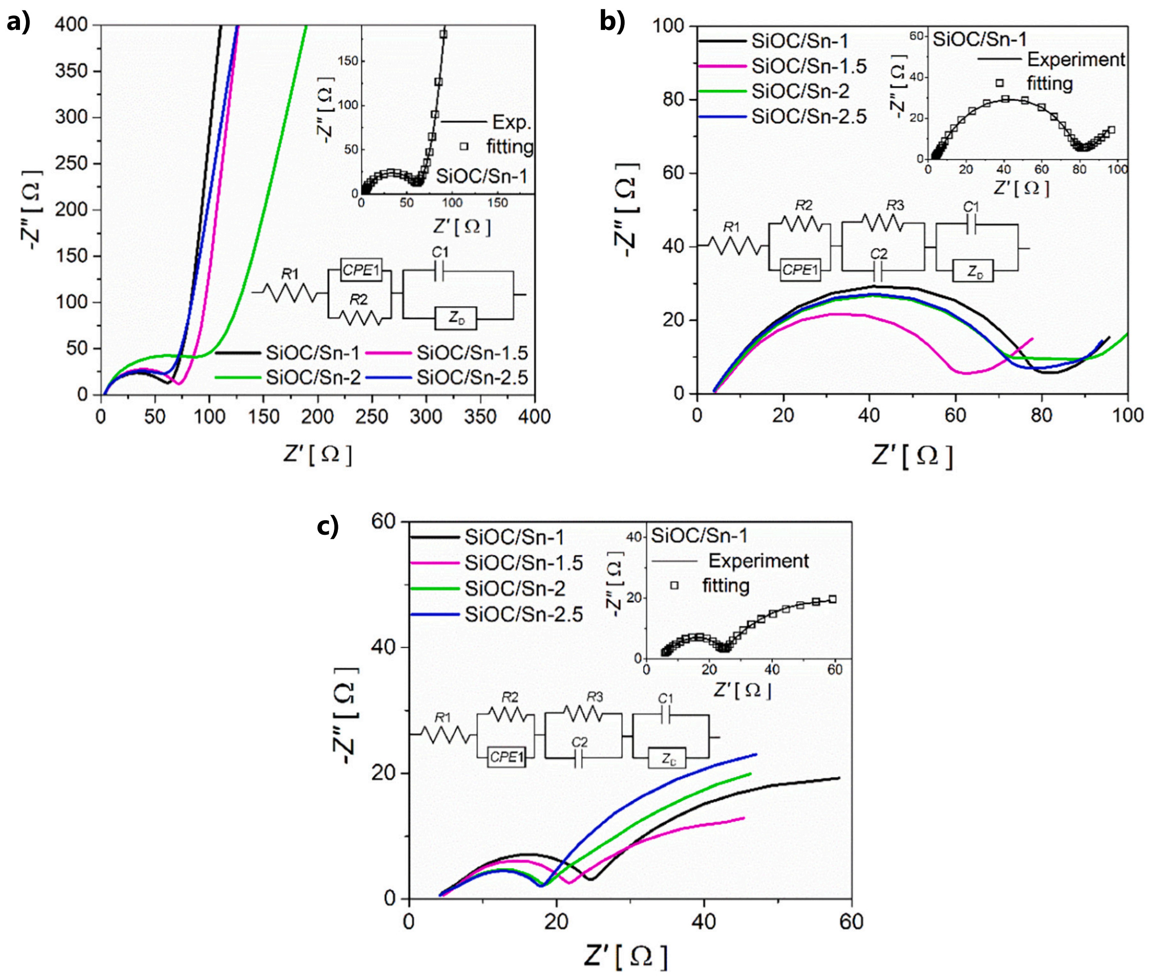

**Fig. 8.** Nyquist plots of the SiOC/Sn$_x$ nanocomposites, electric equivalent circuits and examples of fitted data in Insets of: a) fresh samples, stand-by potential $Es = 3.0$ V (vs. Li/Li$^+$); b) after the first lithiation process, $E = 0.15$ V (vs. Li/Li$^+$); c) lithiated samples after 50 cycles, $E = 0.15$ V (vs. Li/Li$^+$).

improve it. However, taking into account recent reports on the prelithiation methods, low FCE should not be a considered a serious issue for modern anode materials [29].

Fig. 9c and Table 3 show the cycling stability performance of SiOC/Sn$_x$ nanocomposites charged/discharged with at a constant current of 372 mA g$^{-1}$ within a potential range of 5 mV – 1.5 V. The potential range for these tests was chosen with commercial application. The nanocomposites exhibit high capacities, reaching 500 mAh g$^{-1}$ after 100 cycles, and satisfactory stability. The capacities are similar for all of the studied SiOC/Sn$_x$, but the highest values were recorded for the SiOC/Sn-2 sample. These results suggest that further increase of tin content in the material does not provide any additional benefits. The SiOC/Sn-2 sample was selected for extended cycling (400 charge/discharge cycles at 372 mA g$^{-1}$ in the potential range 5 mV – 3.0 V), shown in Inset in Fig. 9c. In this test, the initial two and the last two cycles were measured at a low current density of 18.6 mA g$^{-1}$ to establish a stable SEI and to check if the capacity value is maintained after 400 cycles at a higher current rate. The capacity values achieved in the broader voltage range (5 mV – 3.0 V) are higher but on the other hand the capacity drop is bigger than for the lower potential range (5 mV – 1.5 V). The fastest capacity drop is observed in the first 50 cycles, then the capacity decay is very slow. After 400 cycles in the potential range of 10 mV – 3 V, the SiOC/Sn-2 nanocomposite exhibits excellent specific capacities of 650 and 750 mAh g$^{-1}$ at current density of 372 and 18.6 mA g$^{-1}$, respectively. The capacity retention at 372 mA g$^{-1}$ after 400 cycles reaches 81 %, which shows a better performance than earlier reports which obtained 73.5 % after 200 cycles [12] and 81 % after 100 cycles, and farther degradation after 180 cycles [6].

It is worth to note the excellent performance of the SiOC/Sn nanocomposites in the rate capability tests (Fig. 9d and Table 4). All of the materials exhibit outstanding capacity retention of ~80–90 % when the current is increased from 74 mA g$^{-1}$ to ~1.5 A g$^{-1}$, and high capacity values reaching 544 mAh g$^{-1}$ at ~1.5 A g$^{-1}$. After the reduction of the current to 74 mA g$^{-1}$ the capacity returns to the previous level. These results contrast with earlier reports on SiOC/Sn$_x$ [28] which showed capacity degradation after 100 cycles at 74 mA g$^{-1}$ These results indicate that the electrical contact between silicon oxycarbide and tin is better preserved after cycling at high currents, which is supported by the impedance data.

## 5. Conclusions

In summary, a new and cost-effective preceramic polymer system was developed as a single source precursor for SiOC/Sn$_x$ nanocomposites that can be used as anode materials in Li-ion batteries. The type of polysiloxanes used in this study has a low production cost, which is only about 10 % of the commercial cost of other siloxanes on the market today. A newly developed functional polysiloxanes was combined with an oxygen-rich Sn precursor, tin dioleate, Sn(Ole)$_2$, which has long carbon chain and is a source of Sn as well as C. Pyrolysis of this cross-linked preceramic which different wt% of Sn(Ole)$_2$ in an argon atmosphere led to the formation of polymer-derived SiOC/Sn$_x$ nanocomposites. The final ceramic nanocomposite contains nano-sized Sn distributed within an amorphous SiOC matrix. Electrochemical

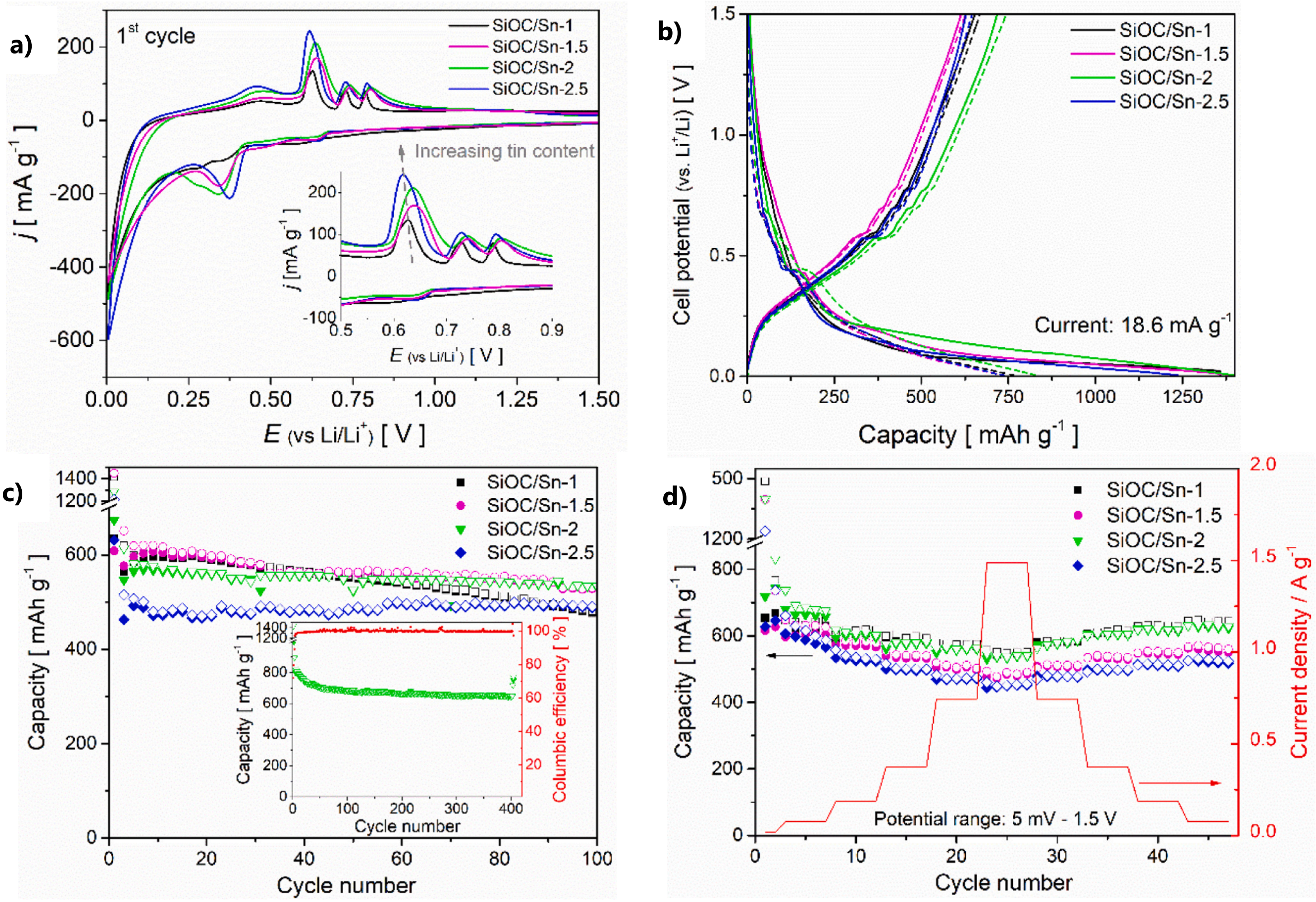

**Fig. 9.** Electrochemical performance of SiOC/Sn$_x$ nanocomposites: a) Cyclic voltammetry curves (second cycle, 0.1 mV s$^{-1}$), b) galvanostatic charge–discharge curves: 1st charge-discharge cycle - solid lines, 2nd cycle – dashed lines, current density 18.6 mA g$^{-1}$, c) cycling stability (at 372 mA g$^{-1}$, voltage range 5 mV-1.5 V, lithiation with constant current-constant voltage (CC-CV), delithiation CC), inset: prolonged stability test for SiOC/Sn-2 sample (at 372 mA g$^{-1}$, voltage range 5 mV-3.0 V, lithiation with CC-CV, delithiation CC), d) rate capability (voltage range 5 mV-1.5 V, lithiation with constant current-constant voltage (CC-CV), delithiation CC).

**Table 3**
Electrochemical data of the charging and discharging of the SiOC/Sn$_x$ nanocomposites (potential range 5 mV–1.5 V).

| SiOC/Sn$_x$ | Initial delithiation [mAh g$^{-1}$] | Initial lithiation [mAh g$^{-1}$] | Average capacity of 100 cycles at 372 mA g$^{-1}$ [mAh g$^{-1}$] | | First cycle efficiency [%] |
|---|---|---|---|---|---|
| | | | Delithiation | Lithiation | |
| SiOC/Sn-1 | 653 | 1488 | 462 | 466 | 43.9 |
| SiOC/Sn-1.5 | 614 | 1396 | 454 | 435 | 44.0 |
| SiOC/Sn-2 | 717 | 1399 | 506 | 507 | 51.3 |
| SiOC/Sn-2.5 | 627 | 1238 | 489 | 492 | 50.6 |

characterization of the materials using Li-ion half cells revealed capacities in the range of 650–750 mAh g$^{-1}$. The cells showed good cycling stability with capacity retention of more than 80 % after cycling. The methodology reported here for the synthesis of single source precursors opens an unlimited space for material design at the molecular level. The extended cycling (400 cycles) of the sample SiOC/Sn-2 sample gave promising figures that predict the possibility of its materialization in the future. Future work should focus on investigation and optimizing methods to reduce irreversible capacity losses by tailoring the molecular composition of the starting precursors. The concept of using such a precursor-derived matrix can be extended to other high capacity alloy materials and can be used to stabilize the high capacity performance of novel Si-based anodes.

**Table 4**
Rate capability data of the SiOC/Sn$_x$ nanocomposites (potential range 5 mV–1.5 V).

| SiOC/Sn$_x$ | Capacity regained at 74 mA g$^{-1}$ [mAh g$^{-1}$] | Capacity regained at 1488 mA g$^{-1}$ [mAh g$^{-1}$] | Capacity retention ($C_{1488\ mA\ g\text{-}1}/C_{74\ mA\ g\text{-}1}$) [%] |
|---|---|---|---|
| SiOC/Sn-1 | 615 | 544 | 88.5 |
| SiOC/Sn-1.5 | 602 | 483 | 80.2 |
| SiOC/Sn-2 | 663 | 534 | 80.5 |
| SiOC/Sn-2.5 | 588 | 448 | 76.2 |

## Funding

The NMR spectrometer was funded in part by grant SNF-150638 from the Swiss National Science Foundation.

## CRediT authorship contribution statement

**Gurdial Blugan:** Writing – review & editing, Supervision, Conceptualization, Writing – original draft. **Natalia Kovalska:** Writing – original draft, Validation, Methodology, Investigation, Formal analysis, Conceptualization. **Dominik Knozowski:** Methodology, Investigation. **Pradeep V.W. Sasikumar:** Writing – original draft, Validation, Methodology, Investigation, Conceptualization. **Wim J. Malfait:** Formal analysis. **Silvia Paz:** Formal analysis. **Piotr Madajski:** Formal analysis. **Mateusz Leśniewski:** Formal analysis. **Mirosław Sawczak:** Formal analysis. **Balanand Santhosh:** Writing – review & editing, Validation. **Monika Wilamowska-Zawłocka:** Writing – original draft, Validation, Conceptualization. **Matthias M. Koebel:** Supervision, Methodology, Conceptualization.

## Declaration of competing interest

The authors declare that they have no known competing financial interests or personal relationships that could have appeared to influence the work reported in this paper.

## Data availability

Data will be made available on request.

## Acknowledgments

We thank Daniel Rentsch for access to, and maintenance of, the NMR spectrometer. M.W.-Z. and G.B. acknowledge Gdańsk University of Technology, grant no. DEC-9/1/2022/IDUB/II.1a/Au under the AURUM - 'Excellence Initiative - Research University' program.

## Appendix A. Supplementary data

Supplementary data to this article can be found online at https://doi.org/10.1016/j.est.2024.111676.

## References

[1] R. Sujith, J. Gangadhar, M. Greenough, R.K. Bordia, D.K. Panda, A review of silicon oxycarbide ceramics as next generation anode materials for lithium-ion batteries and other electrochemical applications, J. Mater. Chem. A 11 (2023) 20324–20348, https://doi.org/10.1039/d3ta01366a.

[2] K. Edström, M. Herstedt, D.P. Abraham, A new look at the solid electrolyte interphase on graphite anodes in Li-ion batteries, J. Power Sources 153 (2006) 380–384, https://doi.org/10.1016/j.jpowsour.2005.05.062.

[3] Y. Wang, J.Y. Lee, T.C. Deivaraj, Tin nanoparticle loaded graphite anodes for Li-ion battery applications, J. Electrochem. Soc. 151 (2004) A1804, https://doi.org/10.1149/1.1799491.

[4] X. Jin, A. Vora, V. Hoshing, T. Saha, G. Shaver, R.E. García, O. Wasynczuk, S. Varigonda, Physically-based reduced-order capacity loss model for graphite anodes in Li-ion battery cells, J. Power Sources 342 (2017) 750–761, https://doi.org/10.1016/j.jpowsour.2016.12.099.

[5] S. Bin Mujib, G. Singh, Polymer derived SiOC and SiCN ceramics for electrochemical energy storage: a perspective, Int. J. Ceram. Eng. Sci. 4 (2022) 4–9, https://doi.org/10.1002/ces2.10108.

[6] R.J.C. Dubey, P.V.W. Sasikumar, F. Krumeich, G. Blugan, J. Kuebler, K. V. Kravchyk, T. Graule, M.V. Kovalenko, Silicon oxycarbide—tin nanocomposite as a high-power-density anode for Li-ion batteries, Adv. Sci. 6 (2019), https://doi.org/10.1002/advs.201901220.

[7] J. Kaspar, C. Terzioglu, E. Ionescu, M. Graczyk-Zajac, S. Hapis, H.J. Kleebe, R. Riedel, Stable SiOC/Sn nanocomposite anodes for lithium-ion batteries with outstanding cycling stability, Adv. Funct. Mater. 24 (2014) 4097–4104, https://doi.org/10.1002/adfm.201303828.

[8] M.N. Obrovac, V.L. Chevrier, Alloy negative electrodes for Li-ion batteries, Chem. Rev. 114 (2014) 11444–11502, https://doi.org/10.1021/cr500207g.

[9] D. Liu, Z. jiao Liu, X. Li, W. Xie, Q. Wang, Q. Liu, Y. Fu, D. He, Group IVA Element (Si, Ge, Sn)-based alloying/dealloying anodes as negative electrodes for full-cell Lithium-ion batteries, Small 13 (2017) 1–27, https://doi.org/10.1002/smll.201702000.

[10] G. Li, S. Guo, B. Xiang, S. Mei, Y. Zheng, X. Zhang, B. Gao, P.K. Chu, K. Huo, Recent advances and perspectives of microsized alloying-type porous anode materials in high-performance Li- and Na-ion batteries, Energy Mater. 2 (2022) 200020, https://doi.org/10.20517/energymater.2022.24.

[11] M.T. McDowell, S.W. Lee, W.D. Nix, Y. Cui, 25th anniversary article: understanding the lithiation of silicon and other alloying anodes for lithium-ion batteries, Adv. Mater. 25 (2013) 4966–4985, https://doi.org/10.1002/adma.201301795.

[12] S. Eun Wang, J.S. Park, M. Ji Kim, Y. Chan Kang, D. Soo Jung, One-pot spray pyrolysis for core–shell structured Sn@SiOC anode nanocomposites that yield stable cycling in lithium-ion batteries, Appl. Surf. Sci. 589 (2022), https://doi.org/10.1016/j.apsusc.2022.152952.

[13] M. Halim, C. Hudaya, A.Y. Kim, J.K. Lee, Phenyl-rich silicone oil as a precursor for SiOC anode materials for long-cycle and high-rate lithium ion batteries, J. Mater. Chem. A 4 (2016) 2551–2556, https://doi.org/10.1039/c5ta09973k.

[14] C. Stabler, E. Ionescu, M. Graczyk-Zajac, I. Gonzalo-Juan, R. Riedel, Silicon oxycarbide glasses and glass-ceramics: "All-Rounder" materials for advanced structural and functional applications, J. Am. Ceram. Soc. 101 (2018) 4817–4856, https://doi.org/10.1111/jace.15932.

[15] R.J.C. Dubey, P.V.W. Sasikumar, N. Cerboni, M. Aebli, F. Krumeich, G. Blugan, K. V. Kravchyk, T. Graule, M.V. Kovalenko, Silicon oxycarbide-antimony nanocomposites for high-performance Li-ion battery anodes, Nanoscale 12 (2020) 13540–13547, https://doi.org/10.1039/d0nr02930k.

[16] W. Guo, O. Icin, C. Vakifahmetoglu, D. Kober, A. Gurlo, Magnesium-ion Battery Anode from Polymer-derived SiOC Nanobeads. doi:https://doi.org/10.1002/adfm.202304933 (n.d.).

[17] A.N.M. Koebel, A. Stojanovic, W.J. Malfait, Method for Preparing a Siloxane Based Polymeric Liquid Material and Materials Made Therefrom, 2019.

[18] X. Zhu, M. Jaumann, K. Peter, M. Möller, C. Melian, A. Adams-Buda, D.E. Demco, B. Blümich, One-pot synthesis of hyperbranched polyethoxysiloxanes, Macromolecules 39 (2006) 1701–1708, https://doi.org/10.1021/ma052179+.

[19] W.J. Malfait, R. Verel, M.M. Koebel, Hydrophobization of silica aerogels: insights from quantitative solid-state NMR spectroscopy, J. Phys. Chem. C 118 (2014) 25545–25554, https://doi.org/10.1021/jp5082643.

[20] I.S. Protsak, Y.M. Morozov, W. Dong, Z. Le, D. Zhang, I.M. Henderson, A 29Si, 1H, and 13C solid-state NMR study on the surface species of various depolymerized organosiloxanes at silica surface, Nanoscale Res. Lett. 14 (2019), https://doi.org/10.1186/s11671-019-2982-2.

[21] A. Sadezky, H. Muckenhuber, H. Grothe, R. Niessner, U. Pöschl, Raman microspectroscopy of soot and related carbonaceous materials: spectral analysis and structural information, Carbon N. Y. 43 (2005) 1731–1742, https://doi.org/10.1016/j.carbon.2005.02.018.

[22] Å. Björkman, Thermische Klärschlammbehandlung, Schweizerische Zeitschrift Für Hydrol. 31 (1969) 632–645, https://doi.org/10.1007/BF02543692.

[23] B. Dippel, H. Jander, J. Heintzenberg, NIR FT Raman spectroscopic study of flame soot, Phys. Chem. Chem. Phys. 1 (1999) 4707–4712, https://doi.org/10.1039/a904529e.

[24] A. Cuesta, P. Dhamelincourt, J. Laureyns, A. Martínez-Alonso, J.M.D. Tascón, Raman microprobe studies on carbon materials, Carbon N. Y. 32 (1994) 1523–1532, https://doi.org/10.1016/0008-6223(94)90148-1.

[25] D. Knozowski, P. Vallachira Warriam Sasikumar, P. Madajski, G. Blugan, M. Gazda, N. Kovalska, M. Wilamowska-Zawłocka, Material design and optimisation of electrochemical Li-ion storage properties of ternary silicon oxycarbide/graphite/tin nanocomposites, Nanomaterials 12 (2022), https://doi.org/10.3390/nano12030410.

[26] J.L. Lorie Lopez, P.J. Grandinetti, A.C. Co, Phase transformations and capacity fade mechanism in Li x Sn nanoparticle electrodes revealed by operando 7 Li NMR, J. Mater. Chem. A 7 (2019) 10781–10794, https://doi.org/10.1039/C9TA03345A.

[27] M. Graczyk-Zajac, L. Toma, C. Fasel, R. Riedel, Carbon-rich SiOC anodes for lithium-ion batteries: part I, Influence of material UV-pre-treatment on high power properties, Solid State Ionics. 225 (2012) 522–526, https://doi.org/10.1016/j.ssi.2011.12.007.

[28] D. Knozowski, P.V.W. Sasikumar, R. Dubey, M. Aebli, K.V. Kravchyk, G. Trykowski, M.V. Kovalenko, T. Graule, M. Wilamowska-Zawłocka, G. Blugan, Silicon oxycarbide-tin nanocomposite derived from a UV crosslinked single source preceramic precursor as high-performance anode materials for Li-ion batteries, Appl. Mater. Today 27 (2022) 101424, https://doi.org/10.1016/j.apmt.2022.101424.

[29] B. Wang, D. Wang, F. Wang, J. Li, B. Wang, Y. Zhou, H. Liu, S. Dou, Prelithiation: a crucial strategy for boosting the practical application of next-generation lithium ion battery, ACS Nano 15 (2021) 2197–2218, https://doi.org/10.1021/acsnano.0c10664.